JOM Journal of Optical Microsystems

RESEARCH PAPER

Radio-frequency spectrometry based on laser speckle imaging

Matthew J. Kelley,* Thomas Justin Shaw, and George C. Valley
The Aerospace Corporation, El Segundo, California, United States

ABSTRACT. We demonstrate a microwave photonic spectrometer based on laser speckle pattern imaging that has some significant advantages over state-of-the-art electronic technology, including high resolution, multifrequency detection over broad and reconfigurable bandwidths. The spectrometer operates by modulating the radio-frequency (RF) signal on a frequency-stabilized continuous wave (CW) laser using an electro-optic intensity modulator. The modulated CW laser travels through a 100-m long high numerical aperture multimode optical fiber before collection and recording on a camera. To calibrate the spectrometer, an RF tone generator is stepped over the desired operational range of the spectrometer with a frequency step size on the order of the desired frequency resolution while the speckle pattern images are recorded and stored. An unknown signal under test is then generated and recovered from the calibration set using regression analysis techniques. The spectrometer exhibits a 5-MHz resolution with a single-tone recovery accuracy of greater than 99.9% over a 17-GHz frequency range and a mean recovery error below 1 MHz over smaller ranges. We also incorporated a high-speed camera, operated at an 800-kHz frame rate, permitting data collection at speeds commensurate with the best real-time spectrum analyzers. We present the results of our analysis of the spectrum recovery process with the goal of increasing the spectral recovery rate. In addition, in the interest of miniaturization, we present the results of simulations of 50-μm wide and 40-cm long multimode waveguides in silicon nitride and silicon, which suggest that the 100-m long multimode fiber can be replaced by short waveguides without degradation in performance.

Keywords: speckle; instantaneous frequency measurement; microwave photonics; radio-frequency photonics; radio-frequency spectrometer

Paper 23033G received Sep. 28, 2023; revised May 6, 2024; accepted May 21, 2024; published Jun. 25, 2024.

1 Introduction

There is a need to analyze radio-frequency (RF) spectra over an ever-increasing frequency range in the fields of communications, radar detection and warning, signal and electronic intelligence, navigation, space domain awareness, and astronomy, among others.[1–7] Current electronics-based real-time RF/microwave spectrum analyzers have limitations that might be improved through photonic implementations. For example, real-time spectrum analyzers have limited real-time bandwidths ($< \sim 800$ MHz[8]), resolution, and high relative size, weight, power, and cost, resulting from the need to rapidly digitize incoming data and compute fast Fourier transforms to process and store or display the frequency-domain signals of interest. Meanwhile, the instantaneous frequency measurement (IFM) receiver can measure the frequency of a signal of interest over

*Address all correspondence to Matthew J. Kelley, matthew.kelley@aero.org

Table 1 Real-time spectrum analyzer performance as of May 2022.

Instrument/specification	Keysight—N9040B UXA X-Series	Rohde & Schwarz—FSVR40	Tektronix—RSA7100B	Tektronix—RSA5100B
Maximum real-time bandwidth	510 MHz	40 MHz	800 MHz with signals >3.6 GHz	165 MHz
Frequency coverage, base	10 Hz to 50 GHz	100 Hz to 40 GHz	3.6 to 26.5 GHz	1 to 26.5 GHz
Resolution bandwidth	1 to 37 MHz	50 kHz @ full BW (800 frequency steps)	120 Hz to 50 MHz	25 kHz to 20 MHz
Minimum signal duration @ maximum real-time bandwidth	3.33 ns with SNR > 60 dB; 3.51 μs to meet noise floor	25 ns with SNR > 60 dB; 24 μs to meet noise floor	Depends on res. bandwidth; 2.5 μs @ 1 MHz res. bandwidth	Depends on res. bandwidth; 2.7 μs @ 1 MHz res. bandwidth

a very broad bandwidth with an MHz-level resolution, even for signals of very short duration.[9–11] However, state-of-the-art IFM receivers are not able to measure complicated signals, such as those consisting of multiple tones[11] or those with a broad spectrum.[10] See Table 1 for representative real-time spectrum analyzer capabilities.

Photonic measurement of microwave signals promises broader bandwidth, higher spectral resolution, and increased resilience to electromagnetic interference relative to conventional electronic instruments in an equivalent or smaller package with the potential for reduced power consumption.[1–5] Photonic IFM receiver implementations have demonstrated broader bandwidths than their RF equivalents and full photonic integration,[12] but those based on interferometers suffer from the same limitations for broadband or multitone spectra.[5] Other photonic implementations require repetitive signals,[13] slow response or acquisition times,[5,12–16] degraded spectral resolution relative to their RF counterparts,[5,12] or cooling to a few degrees Kelvin.[15,16] The speckle pattern-sensing technique presented in this paper is a novel architecture for microwave spectrum sensing, capable of simultaneous single-MHz resolution, high bandwidth (>17 GHz), high-speed acquisition, and multitone sensing.

The laser speckle pattern-based microwave spectrometer shares many similarities with optical laser speckle imaging spectrometers.[17–35] Rather than matching the input wavelength or energy one-to-one to a spatial location, as is typical in common optical spectrometers employing dispersion or refraction—utilizing a prism or grating, respectively—such spatial "multiplex"[17] spectrometers associate the output spatial patterns of light intensity to wavelength. An advantage is gained in the ability to pick alternate dispersive materials with advantageous properties. In fact, the combination of a photosensor array and any dispersive element can function as a spectrometer to some degree.[36] Early demonstrations suffered from very high insertion loss, poor spectral resolution, and/or unneeded complexity;[17–20] however, in 2012, Redding and Cao[21] demonstrated a multiplex spectrometer in which the primary element was a multimode fiber and low insertion loss and high resolution over relatively broad spectral ranges were featured. Since then, the technique has been performed with different resolutions,[22–26] in compact silicon multimode waveguides,[24] and in tapered fiber.[37]

It is useful to think of a speckle-based spatially multiplexed spectrometer as a system that is calibrated or trained through the creation of a dictionary that associates a characteristic laser speckle (spatial optical intensity) pattern to calibration wavelengths over the operating range of the device. If the transmission matrix does not change, this dictionary can be used to recover an unknown spectrum. However, in practice, slow changes to the environment of the transmission medium necessitate periodic reacquisition of calibration data, though correlation may be maintained for periods of hours by employing careful environmental controls.[25]

Another significant advantage of the speckle-based spectrometer, relative to a conventional optical spectrometer, is that the multiplex speckle spectrometer does not suffer from signal interference from higher diffraction orders and can be used over greater than an octave of bandwidth without the complication of order-sorting filters. There is no free spectral range effect. In fact, it is

possible to calibrate the spectrometer on an unevenly spaced frequency grid, i.e., only at wavelengths or frequencies of interest, or with different resolutions over different regions of the bandwidth of the device. In the RF domain, this also means that the device can read out high-frequency signals without necessitating GHz-rate analog to digital converters or frequency mixers.

Unlike conventional optical spectrometers, the output of a speckle spectrometer generally does not have a one-to-one mapping to any coordinate, even upon transformation. Thus, the spectrum of interest must be computed, typically using minimization algorithms, from the digitized speckle pattern. Thus, there has been considerable effort in the development of recovery algorithms. Some techniques that have been explored include transmission matrix inversion,[21–24,26] truncated singular value decomposition (SVD),[21–24] other regularization methods,[24] principal component analysis,[27,28] computational neural networks, and deep learning[29–31] to reduce the effect of environmental noise. The work presented here also has similarities to the recovery of sparse RF signals in optical compressive sensing.[32–35,38] Some of the recovery algorithms tested for spectrum recovery are summarized in Sec. 3.

2 Experimental

This section describes the experimental realization of the speckle-based RF spectrometer. Section 2.1 describes modifications of the setup to support high-speed operation.

Figure 1 shows the experimental layout of the RF spectrometer. A 780 nm laser (Toptica DL780 Pro, Pittsford, New York, United States) was frequency stabilized with a compact saturated absorption spectroscopy (CoSY, TEM Messtechnik GmbH, Hannover, Germany) package to a rubidium D_2 hyperfine transition. The laser was modulated by a null-biased electro-optic intensity modulator that was driven by an RF signal generator, which played single tones during the calibration process or generated the signal under test (SUT). The output of the modulator (<300 nW at 5 ms exposure time) was coupled to a 100-m long, 0.39-numerical aperture, 200-μm core diameter, multimode fiber (Thorlabs FT200EMT, Newton, New Jersey, United States). A 5-m graded index multimode fiber and mode-scrambler (Newport FM-1, Newcastle, Washington, United States) were inserted to better populate all modes of the multimode fiber. The output of the graded index fiber was fusion-spliced to the input of the larger-core step-index multimode fiber for stability. The step-graded-step scrambler was found to be ineffective at populating the modes of the 100-m fiber; however, the mode scrambler was found to be effective. The image of the speckle pattern noticeably expanded in size and was attenuated in amplitude as the mode scrambler was tightened. The spectral correlation width was also significantly reduced.

More than 98 meters of the 100-m multimode fiber were potted in an aluminum baseplate and held in contact with a large optical table to reduce the effects of variations in temperature and vibrations. The entire fiber assembly was stored in a sealed box to reduce the influence of air currents. At the exit of the fiber, the light was collected by a lens and coupled to the active region

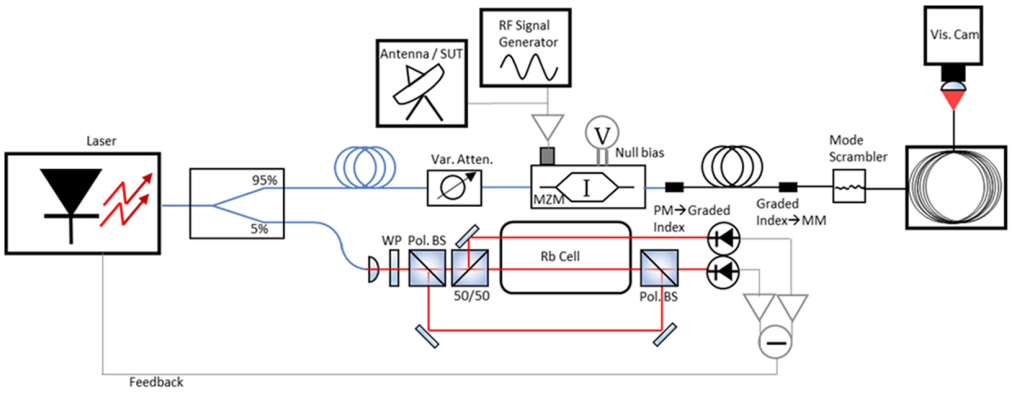

Fig. 1 Diagram of the experimental apparatus. A frequency-stabilized laser is modulated by an RF calibration source or SUT. The modulated laser is transmitted through 100 m of multimode fiber before imaging on a camera.[39,40]

(typically 256×256 pixels) of a laboratory sCMOS camera (Thorlabs CS2100M-USB, except where otherwise noted).

2.1 High-Speed Operation

To demonstrate high-speed data acquisition, the standard laboratory camera was replaced with a high-speed camera (Photron FASTCAM Nova S6, monochrome). A 128×16 pixel window was selected, which resulted in operation at a rate of 800,000 frames per second and an approximate integration time of 1 μs. With respect to the previous setup, the focus of the lens system was changed, so more speckle features were imaged onto the smaller active region of the camera. In this mode of operation, the laser power at the output of the modulator was measured to be 22 μW, which corresponded to operation safely below the pixel saturation threshold. Meanwhile, a microwave frequency generator (HP 8340B) sweeper was repeatedly swept from 2 to 7 GHz at a rate of 555 GHz/second. A complete scan consisted of 7711 images, and each scan was recorded in ~9 ms of lab time.

3 Data Processing and Signal Recovery

The spectrum of the SUT is not linearly encoded on the speckle pattern and must be recovered using computation. This section begins with a description of the data acquisition and storage process and concludes with a discussion of various signal recovery techniques that were employed.

3.1 Data Collection

During the calibration process, a sequence of equally spaced RF tones is played over the operation range of interest, in which the frequency spacing of the tones is typically set to the resolution of interest. While each tone is being played, a two-dimensional array from the camera—the speckle image—is recorded, converted to a one-dimensional array, and saved. The full set of these arrays is the calibration matrix and serves as the dictionary for recovery. Finally, one or more signals of interest are applied to the same setup, and the data array is stored.

3.2 Spectrum Recovery

After both the calibration dictionary and the signal of interest are acquired and stored, the spectrum of interest must be computationally reconstructed. We have primarily explored regression analyses to determine the spectrum of the unknown signal.

Regression analysis seeks to estimate the relationship between dependent and independent variables. In this case, the dependent variables are the spectral coefficients scaling the recorded pixel intensities of each frequency component of the dictionary to the measured pixel intensities of the SUT. The data coefficient matrix (dictionary), X, is composed of N measurements (columns, frequencies), consisting of M elements (rows, pixel intensities) each. In most cases presented here, $M > N$, and the system is overdetermined. Although this is not true in some of the cases discussed in Sec. 4, such as that of the high frame rate camera, the same data processing procedure was used for consistency.

Before regression analysis, each calibration and SUT frequency dataset is set to have zero mean. Ordinary least squares is found to perform poorly in the presence of experimental noise and returns too many nonzero spectral coefficients. Thus, we initially begin our analysis by focusing on the lasso (penalized l^1-norm) algorithm[41] because it promotes sparsity in the number of returned nonzero spectral coefficients with an appropriate choice of the tuning parameter, α, that controls the size of the regularization term in lasso, relative to the measurement constraint. However, lasso performs slowly when the system is overdetermined, so to reduce the computational time, the SVD of the data coefficient matrix X is used to reduce the size of the problem. X is decomposed into three matrices as

$$X = U * S * V^T, \tag{1}$$

where U and V are orthogonal and S is a "main diagonal" matrix composed of zeros and the so-called singular values (SVs), as shown in Fig. 2. Because there are only N singular values, a large fraction of S is composed of zeros, and thus, we can truncate U to include only the

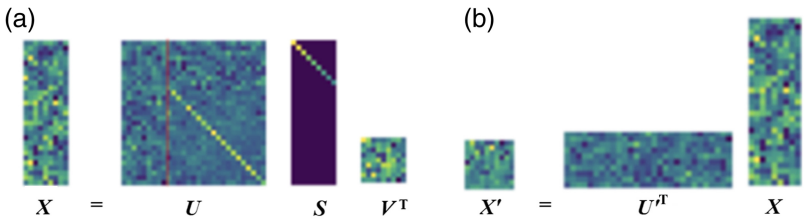

Fig. 2 (a) SVD of the calibration matrix. (b) Projection of the calibration data onto the space spanned by the calibration measurements.[39,40]

first N columns. The new matrix is called U'. It is used to reduce the dimensionality of X by projection [see Fig. 2(b)]:

$$X' = U'^{T} * X, \tag{2}$$

which also projects the data from the SUT to the same subspace. There is no loss of information in this transformation, and the increase in recovery speed using X' depends on the number of pixels and dictionary elements used but is often several orders of magnitude. The speed and recovery accuracy can be further improved with additional truncation by selecting only those columns of U corresponding to the most significant singular values, or principal components,[27,28] which reduces the matrix multiplication time and results in a faster spectrum recovery. It also has the effect of reducing the recovery error as this operation has a spectral domain low-pass filtering effect when the number of columns of U is reduced. However, the technique requires careful tuning of the number of SVs to limit the excessive reduction of the correlation width that, in turn, limits the resolution and dynamic range of the spectrometer.

After performing the SVD, it is instructive to look at the Pearson autocorrelation coefficients of the dictionary to determine the correlation width of the dictionary. See Fig. 3 for an example. The cross-correlation coefficients between the dictionary and SUT data set(s) can also be computed to judge the stability of recovery. If the SUT is composed of a single frequency, such as the typical scenario in which an IFM receiver is used, the maximum of the correlation function serves as the recovered frequency. Computing the correlation coefficient maximum is considerably faster than a lasso computation and provides the same result.

The spectrum can be more finely recovered using lasso or elastic-net (a regression that incorporates L1 and L2 norm penalties) regressions,[42] selectively tailoring α to promote sparsity in the number of positive spectral coefficients relative to ordinary least squares ($\alpha = 0$). However, this process can be slow and requires user input or automation to correctly predict the spectrum. Lasso-based recovery becomes problematic when the SUT has multiple frequency components, particularly when they are not of the same intensity. The frequency accuracy of recovered spectral components is also affected when multiple components are spaced more closely than the correlation width of the spectrometer. For these reasons, we employed orthogonal matching

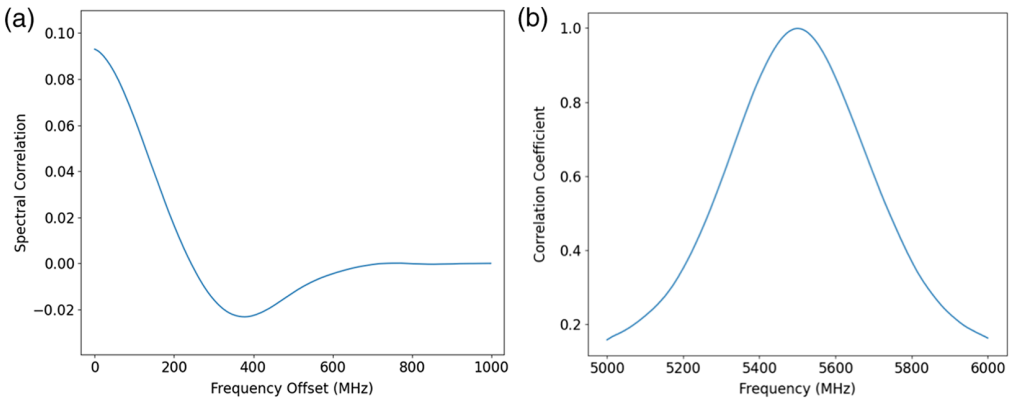

Fig. 3 (a) Spatially averaged spectral correlation function.[22] (b) Auto correlation coefficient of a dictionary element at 5500 MHz.[39,40]

pursuit (OMP)[42,43] when signals are composed of multiple frequency components. See Sec. 4 for further details.

4 Results and Analysis

The correlation width can be determined from the correlation analysis as described in Sec. 3, or it can be spatially averaged.[22] Such a spatially averaged spectral correlation plot is shown in Fig. 3(a). The autocorrelation of a signal in the center of the dictionary range is shown in Fig. 3(b). The correlation width, in either case, is 100 s of MHz wide, as judged from the full width at half maximum. However, the spectrometer can discriminate the frequency of input RF spectra far below this width, limited by the signal-to-noise ratio and stability of the setup.

It is instructive to measure the same calibration set of signals (i.e. the "dictionary") in succession as a measure of system performance and resolution. Any deviation in recovery from the diagonal, such as seen in Fig. 4, is a measure of inaccuracy or instability in the system. The wideband dataset, acquired with the slower frame rate camera, varies by an average of much less than 5 MHz (the frequency step size) over the full measurement range (1 to 18 GHz). There are only two one-step recovery errors over the 3196-point range. All other points are recovered along the diagonal and have errors of less than 5 MHz. Figure 4(b) shows a dataset with a 1 MHz step size over a 1 GHz range. There are many more recovery errors relative to the previous set, but the average error in recovery in this dataset is less than 1 MHz (1 step).

4.1 Recovery Speed Improvements

In the interest of increasing the data processing and recovery speed, a smaller subset of pixels is randomly chosen. As expected, the time to compute the SVD, the most computationally expensive task in recovery, drops rapidly as the number of pixels is reduced. Although a full SVD is only required whenever a new dictionary is measured, the time for a matrix multiplication, required every time a spectrum is determined, also scales similarly with the number of pixels, but the time required is small and poorly determined due to large relative variations in computation time among tests (Fig. 5).

The instrument speed increases as the number of pixels is reduced, whereas the dynamic range of the instrument and the recovery accuracy, to a lesser extent, suffer due to lower cross-correlation contrast as a result of using fewer measurements. See Fig. 6.

Not all pixels are equally well suited for use in recovery. As shown in Fig. 7, some pixels have significantly higher spectral correlation maxima than the mean. The use of pixels above the correlation maximum mean provides better recovery than the use of all pixels and is much better compared with those below the mean. See Fig. 8 for a comparison.

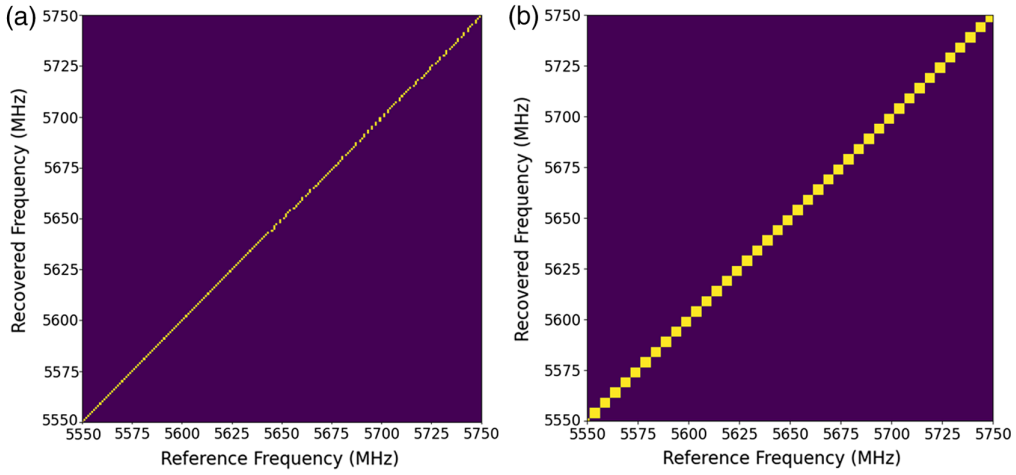

Fig. 4 (a) Recovered frequency for a segment of a 1-GHz dataset from a dictionary with the same parameters (1-MHz spacing). Some recovery errors are observed. (b) Recovered frequency for a segment of a 17-GHz dataset from a dictionary with the same parameters (5-MHz spacing). No recovery errors are observed.[39]

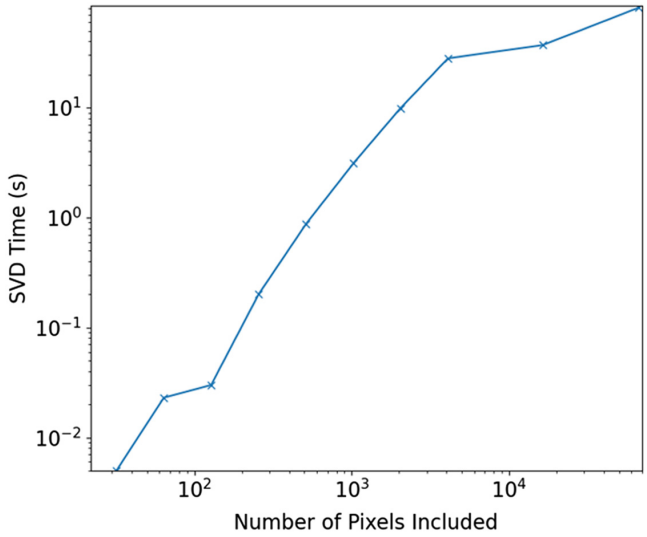

Fig. 5 Time to compute the SVD versus the number of pixels included in the recovery, for a 1000-frequency dataset with a maximum of 65,356 pixels. The computation time is not standardized and is subject to some amount of variation.[40]

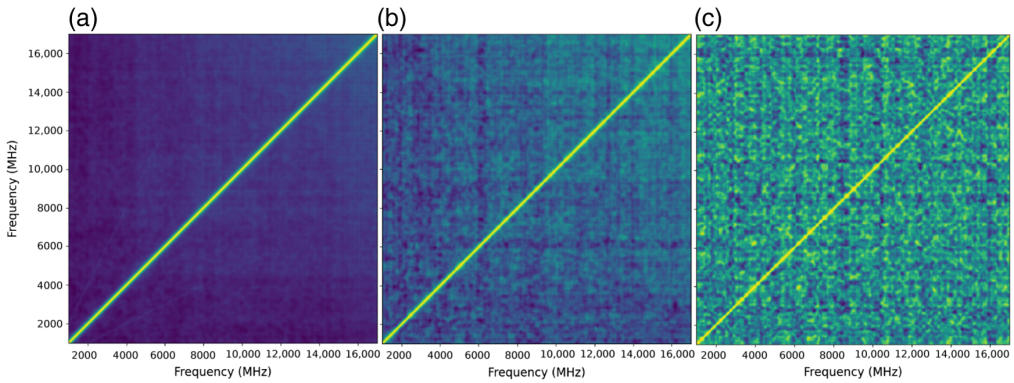

Fig. 6 Cross-correlation plots used for recovery with (a) 66,820, (b) 2048, and (c) 64 randomly selected pixels.[40]

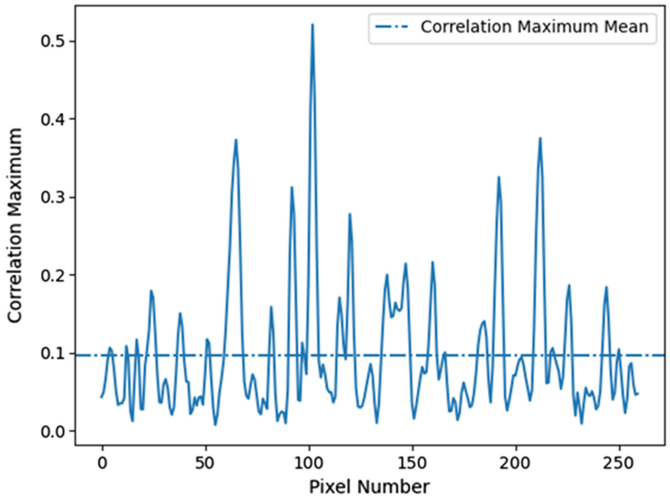

Fig. 7 Spectral correlation maxima along a randomly selected row of pixels with a dashed mean.[40] The dataset is the same as Fig. 3(a).

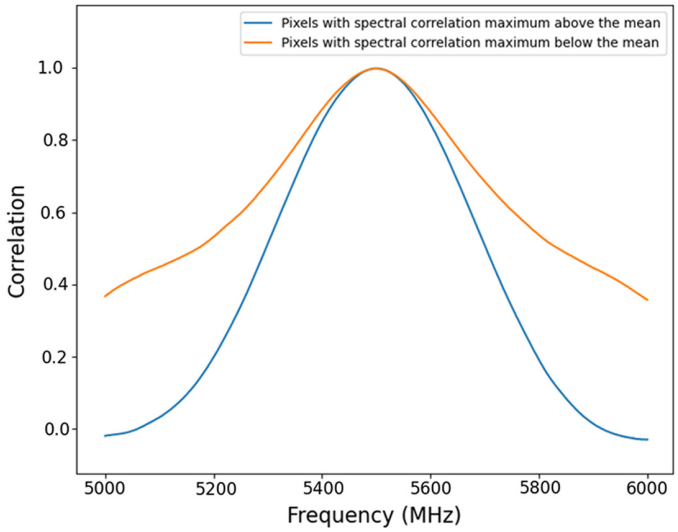

Fig. 8 Recovery of a tone at 5500 MHz using only pixels with spectral correlation function maxima above (blue) and below (orange) the mean.

If the "good" pixels can be expeditiously identified, then the downsides of using a lower number of pixels can be offset. The locations of the good pixels do not depend on the RF signal but may be changed by variable environmental conditions. The pixel-by-pixel correlation can be calculated as described in Ref. 2, but this is computationally expensive and slow; however, a pixel's maximum of the spectral correlation function was found to have a positive association with the variance of the values that the pixel takes as frequency is varied during a calibration scan. Unfortunately, high variance does not guarantee a strong correlation; thus, selection by variance does not considerably increase the recovery accuracy. However, a selection of pixels with variance above the mean decreased the computation time by 70%, similar to selection by correlation maximum, and had nearly the same recovery accuracy relative to a computation using the full dataset. Selection by correlation maximum increased recovery by 10% relative to the full dataset.

4.2 Recovery of Multitone Spectra

Figure 9 shows the recovery in the presence of multiple tones. Lasso regression struggles to recover the correct frequencies when two or more tones are positioned within the correlation width of the spectrometer and incorrectly recovers the frequency lower tone (2250 MHz). The situation is more promising when the tones are spaced farther than the correlation width of the spectrometer; however, an algorithm that varies α until a specified number of positive

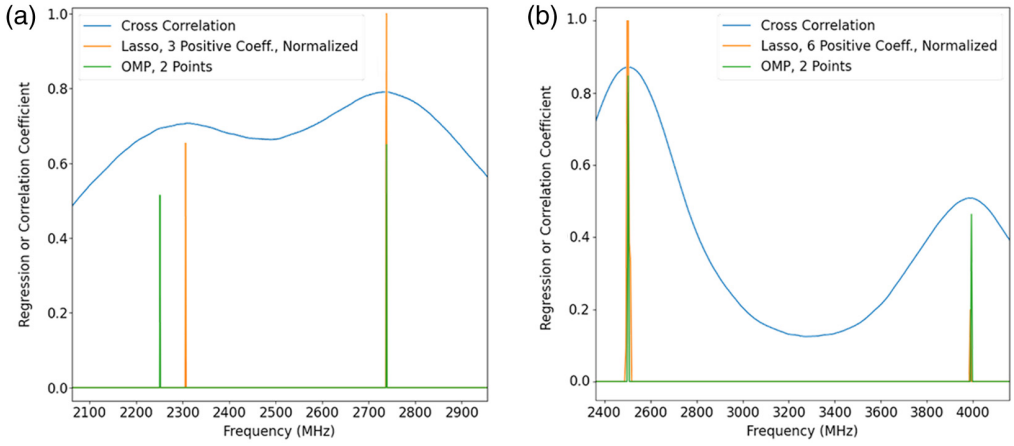

Fig. 9 (a) Comparison of the recovery of multitone (2250 and 2750 MHz) spectra near or below the correlation limit of the spectrometer. (b) Comparison of the recovery of multitone (2500 and 4000 MHz) spectra above the correlation limit of the spectrometer.[39]

coefficients are reached requires more positive coefficients than tones present in the SUT. This results in uncertainty in the recovered tones and incorrect spectral amplitudes. OMP finds the correct tone frequencies in both cases, the correct number of tones, and the appropriate relative amplitudes. Although OMP requires specification of the number of nonzero coefficients or some other stopping criterion, this value can be increased above the number present in the SUT, and extras can be filtered out on the basis of coefficient intensity or sign.

4.3 Experimental Results with a High Frame Rate Camera

The mean recovery error for the data acquired with the high frame rate camera is 1.32 MHz (1.66 MHz, root mean square error) for identical scans in succession, which excludes points at the beginning of the scan when the sweeper is increasing power and has low contrast. This is worse than typical results obtained with the experimental setup using the lower-rate camera (<1 MHz mean recovery error). Also, the dynamic range, related to the correlation floor, is degraded. See Figs. 10 and 7 for illustrative recoveries with the fast camera and the previous camera, respectively. The differences are attributed to the reduced number of pixels in the images (66,820 versus 2048, here), lower bit depth of the saved Photron camera images (could be improved), microwave sweeper settling time and instability, and significantly lower camera integration time.

4.4 Planar Waveguide Speckle Correlation as a Function of Frequency

Multimode planar waveguides have been used by many groups to obtain speckle patterns for optical and RF spectrometers,[24,33,35,44] and they offer the opportunity to make far more compact devices than would be possible with a spool of multimode fiber. It may also be simpler to perform the environmental conditioning (temperature, vibration) needed for a high-resolution spectrometer in a small waveguide. Here, we compare calculations of silicon and silicon nitride waveguide speckle with the speckle observed in our multimode fiber. The best basis for this comparison is the correlation as a function of RF for the pixels of a camera or photodiode array, as shown in Fig. 11. We perform the calculations along the lines described by Ashner et al.,[45] which is essentially an updated version of the standard waveguide solutions from the 1970s. The calculated results assume an optical wavelength of 1550 nm and a 50-μm wide, 40-cm long, single vertical mode planar waveguide in Si or Si_3N_4 with indices of 3.4774 and 1.9963, respectively, and clad by a material with refractive index = 1.44. The waveguides are straight, but clearly for applications, one would spiral or bend the waveguides as in Refs. 24, 33, 35, and 45, which is expected to enhance the speckle mixing. Figure 11(a) shows measured results for the multimode fiber, and Figs. 11(b) and 11(c) show simulations for the Si and Si_3N_4 planar waveguides, respectively. Note that the three families of correlation functions are very similar. This suggests that for the same number of pixels, we should be able to obtain a similar performance for planar waveguides as we obtained for the single mode fiber.

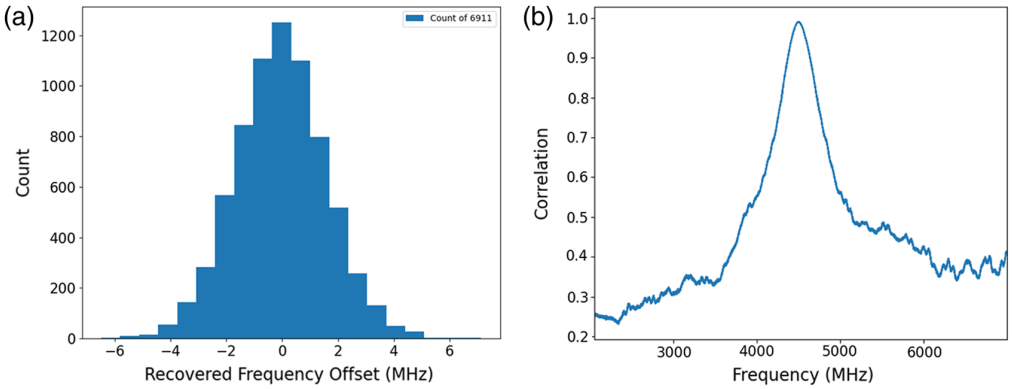

Fig. 10 Recovered frequency offset histogram (a). Correlation plot for a recovered tone at 4500 MHz (b).[40]

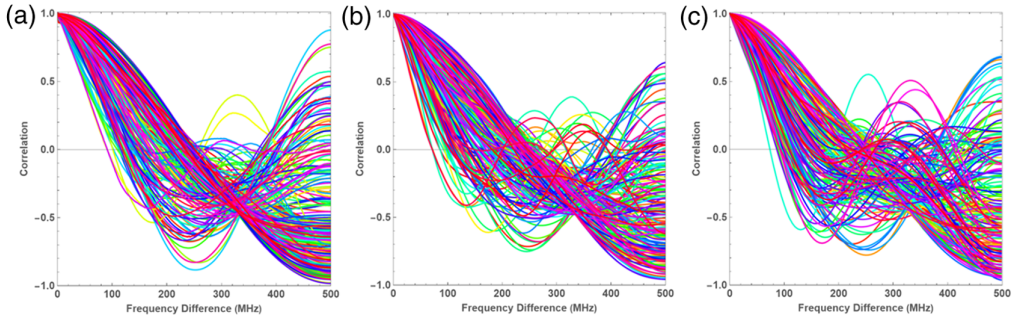

Fig. 11 Correlation as a function of frequency difference. (a) Experimental results for 100 m long multimode fiber at a wavelength of 780 nm. (b) Calculated results for 50 μm wide, 40 cm long Si waveguide at 1550 nm. (c) Calculated results for 50 μm wide, 40 cm long Si_3N_4 waveguide at 1550 nm.[40]

5 Discussion and Conclusions

5.1 Differences between Optical and RF Speckle Spectrometers—Electro-Optic Modulator

The RF speckle spectrometer differs from optical speckle-based implementations in several ways because of the use of an electro-optic modulator (EOM). First, the intensity modulator is a double sideband, and thus, the laser spectrum associated with an RF frequency has multiple spectral components, whereas in most optical spectrometers, a single- or shifted-frequency laser is used to form the calibration set. The optical implementations cannot afford a second sideband unless it is also present in the spectrum of the signal of interest. As a result of the sidebands, the observed speckle patterns in the RF spectrometer may have reduced contrast relative to a single sideband speckle pattern, although the effect should be relatively insignificant for narrowband signals.

Not only is the observed speckle pattern composed of some combination of the upper and lower sidebands, but the residual unextinguished or leaked fundamental laser spectral component contributes to the observed speckle pattern as well. To reduce this effect, a background image was acquired before the calibration step and subtracted from each image to reduce the influence of the leakage power on the image and ultimately to the dynamic range of the spectrometer; however, the residual light still adds to the noise. The experiments reported here employed an EOM with a relatively modest 18 dB extinction ratio. An EOM with a better extinction ratio (optical null depth) could be employed to reduce the intensity of the unmodulated laser fundamental, and EOMs with extinction ratios exceeding 50 dB are commercially available.[46]

The stability of the spectrometer is limited by the time-dependent variation of the null bias point of the Mach-Zehnder modulator. This bias point has a strong influence on the intensity and speckle pattern of the leaked light. When closely examining our longer scans, which had durations of up to 20 min in some cases, the dynamic range, as measured by the ratio of the spectral correlation maximum to correlation minimum, was lower at the end of the scan than at the beginning. Bias drift is a well-known effect in $LiNbO_3$ optical modulators.[47] The voltage required to maintain the optimal bias point tends to drift over time, and this limits the performance of the spectrometer over time. This effect may be mitigated through the use of a modulator bias controller to maintain a high extinction ratio throughout the experiment. This would reduce the time-dependent extinction ratio. The same effect might instead be mitigated through periodic one-null-frame recalibrations. Finally, it is likely possible to minimize the time-dependent optical carrier speckle pattern contribution in post-processing through fitting and subtraction of the slowly varying component.

The RF speckle spectrometer reported here is limited in dynamic range, in part due to the dynamic range of the modulator, as previously discussed, and in part due to the noise of the camera. Even for very short integration or shutter times, there is enough laser power to easily bring the camera near saturation, and thus, the pixel full well depth, read noise, and digitizer bit depth determine the effective dynamic range of the camera. Improvements to any of these aspects improve the performance of the spectrometer. In this light, we tested several cameras throughout our experiments. In fact, our RF speckle spectrometer was first implemented in the optical

C-band,[35,38] but the camera performance was found to be a limiting factor, and this prompted the move to a silicon-compatible wavelength.

We previously discussed the optical leakage effect of the EOM but not the RF dynamic range—RF signals that are too weak do not impart a detectable change to the speckle pattern, and RF signals that are too strong can reduce linearity or cause phase wrap when V_π is exceeded. Increasing the dynamic range of the modulator should help in this regard as well, but other options also exist. This effect might be improved by the addition of an RF limiting amplifier before the EOM or some other form of automated gain control. However, another deleterious effect that limits the dynamic range is the even-order harmonics[48] of the null-biased modulator. These become significant when the applied RF signal power exceeds ~8 dBm and are clearly seen in our data. They are still observable at lower powers but are on the order of the noise in our setup.

5.2 High-Speed Operation

Using a high-speed camera, we were able to increase the data acquisition rate relative to the initial experiments by a factor of 16,000 while only slightly degrading the recovery error. Although the demonstrated 800 kHz acquisition rate is, to the authors' knowledge, the highest rate yet demonstrated for a speckle-based spectrometer, the acquisition rate of the spectrometer can be increased to higher rates using other commercially available cameras, capable of maximum frame rates at MHz rates and with active regions composed of a greater number of pixels.[49] Aside from the greater spectral rate, a more subtle advantage of high-speed operation is that the device might be made more tolerant to environmental and laser frequency drifts over time by rapid reacquisition of the dictionary or tracking of the changes to the speckle pattern over time.[50] This would likely permit the use of a smaller laser, not locked to an atomic reference, further reducing the size, weight, and power of the instrument. In addition, it might remove some of the strict environmental requirements, especially in combination with the smaller, integrated, multimode waveguides discussed in Sec. 4.4, which would be easier to temperature control and would be less susceptible to air currents. Moreover, a photonically integrated device[24] could replace the camera with an integrated high-speed photodiode array to reduce size and improve stability.

The demonstrated increase in data collection speed makes speckle spectrometers competitive with the data rates of real-time spectrum analyzers; however, we were unable to recover spectra at the rate of acquisition. As discussed in Sec. 4.1, reducing the number of pixels used can reduce both recovery and camera frame time; however, this has the effect of increasing the uncertainty in recovery accuracy and lowering the effective dynamic range of the instrument. Improved spectrum recovery algorithms, a real-time operating system, or hardware acceleration might be required for real-time data processing, handling, and storage. A dedicated processor or application-specific integrated circuit would likely help in this regard.

Recently, Murray et al.[50] demonstrated a high-speed time domain spectrometer based on Rayleigh backscattering that is capable of operating at update rates of 385 kHz. Although the measurement speed is limited by the round-trip time in the fiber in these experiments, it could likely support higher rates with a tradeoff in spectral resolution. The disadvantage of this approach is the need for multiple optical amplifiers, which would increase the size, weight, and power of the spectrometer.

5.3 Conclusions

Optically multiplexed RF spectrometers offer many attractive features relative to their electronic counterparts, including high-resolution multiline operation over broad and reconfigurable bandwidths. For example, we used the same speckle-based RF spectrometer over the frequency range of 1 to 18 GHz with calibrated ranges spanning 1 to 17 GHz and resolutions commensurate with the calibration frequency step size, typically between 1 to 5 MHz.[39] These parameters can likely be improved in future iterations, e.g., the operational band could be shifted to millimeter-wave frequencies by frequency mixing or use of a higher bandwidth EOM.[51] The precision and accuracy of recovery can be increased via improvements to (1) the laser's frequency stability, (2) the environment of the multimode fiber, and (3) the null bias point of the EOM, in order of importance. The resolution of the spectrometer can likely reach 10 to 100 s of kHz by laser linewidth

reduction, improved stabilization, or dictionary shifting via speckle pattern tracking.[49] The results of the waveguide simulations in Sec. 4.4 suggest that the spectrometer could be considerably miniaturized by photonic integration and replacement of the multimode fiber with a more dispersive material. Real-time data collection speed comparable to that of the best commercially available microwave real-time spectrum analyzers was demonstrated with the high-speed camera implementation, and this could also be enhanced by integrating the spectrometer.

However, the RF speckle-based spectrometer has some disadvantages with respect to the alternatives. Because this is a computational spectrometer, the spectral information is not directly sensed in the time or frequency domains, and thus, our spectrometer is slower, at least in the current implementation. The RF spectrometer has, and will likely continue to have, a lower dynamic range than alternatives, due in part to both the modulator and the camera. With respect to a conventional spectrometer, a disadvantage of a speckle spectrometer is the difficulty in handling broadband signals. A sufficiently broadband or spectrally dense input signal will remove the contrast of the observed speckle pattern, eventually presenting as a homogenous field. Some progress has been made in measuring broadband signals by employing wavelength division multiplexers and multimode bundles to increase the addressable spectral range for dense signals.[26]

Disclosures

The authors have no financial interest in the work presented here and have no conflicts of interest to disclose.

Code and Data Availability

Data underlying the results presented in this paper are not publicly available at this time but may be obtained from the authors upon reasonable request.

Acknowledgments

The authors wish to thank Matthew Ashner and Radikha Bhuckhory for their contributions to the work presented here. This work was supported under the U.S. Air Force (Contract No. FA8802-19-C-0001).

References

1. X. Zou et al., "Photonics for microwave measurements," *Laser Photonics Rev.* **10**(5), 711–734 (2016).
2. L. R. Cortés et al., "Towards on-chip photonic-assisted radio-frequency spectral measurement and monitoring," *Optica* **7**, 434–447 (2020).
3. D. Marpaung, J. Yao, and J. Capmany, "Integrated microwave photonics," *Nat. Photonics* **13**(2), 80–90 (2019).
4. R. Maram et al., "Recent trends and advances of silicon-based integrated microwave photonics," *Photonics* **6**(1), 13 (2019).
5. L. A. Bui, "Recent advances in microwave photonics instantaneous frequency measurements," *Progr. Quantum Electron.* **69**, 100237 (2020).
6. A. Gambacorta et al., "The Hyperspectral Microwave Photonic Instrument (HyMPI)—advancing our understanding of the Earth's Planetary Boundary Layer from space," in *IGARSS 2022-2022 IEEE Int. Geosci. and Remote Sens. Symp.*, IEEE, pp. 4468–4471 (2022).
7. "Towards more complete space situational awareness—how RF data can fill the gaps in traditional SDA techniques," Kratos Defense & Security Solutions, Inc., https://www.kratosdefense.com/SSA (accessed June 2022).
8. "Tektronix RSA7100B spectrum analyzer datasheet," Tektronix, https://www.tek.com/en/datasheet/rsa7100b-rsa7100b-spectrum-analyzer-datasheet (accessed June 2022).
9. J. P. Coupez et al., "High resolution IFMs," in *14th Int. Conf. Microw., Radar and Wirel. Commun. MIKON - 2002. Conf. Proc. (IEEE Cat.No.02EX562)*, Vol. 2, pp. 484–487 (2002).
10. H. Gruciiala and A. Slowik, "The complex signals instantaneous frequency measurement using multichannel IFM systems," in *15th Int. Conf. Microw., Radar and Wirel. Commun. (IEEE Cat. No.04EX824)*, Vol. 1, pp. 210–213 (2004).
11. J. P. Y. Lee, "Detection of complex and simultaneous signals using an instantaneous frequency measurement receiver," *IEE Proc. F Commun. Radar Signal Process.* **132**(4), 267–274 (1985).
12. Y. Tao et al., "Fully on-chip microwave photonic instantaneous frequency measurement system," *Laser Photonics Rev.* **16**(11), 2200158 (2022).

13. X. Long, W. Zou, and J. Chen, "Broadband instantaneous frequency measurement based on stimulated Brillouin scattering," *Opt. Express* **25**, 2206–2214 (2017).
14. H. Jiang et al, "Wide-range, high-precision multiple microwave frequency measurement using a chip-based photonic Brillouin filter," *Optica* **3**, 30–34 (2016).
15. W. R. Babbitt, "Microwave photonic processing with spatial-spectral holographic materials," *Proc. SPIE* **11296**, 112963L (2020).
16. C. W. Thiel et al., "Optical decoherence and persistent spectral hole burning in Tm^{3+}:$LiNbO_3$," *J. Lumin.* **130**(9), 1598–1602 (2010).
17. R. N. Ibbett, D. Aspinall, and J. F. Grainger, "Real-time multiplexing of dispersed spectra in any wavelength region," *Appl. Opt.* **7**, 1089–1093 (1968).
18. Z. Xu et al., "Multimodal multiplex spectroscopy using photonic crystals," *Opt. Express* **11**(18), 2126–2133 (2003).
19. T. Kohlgraf-Owens and A. Dogariu, "Transmission matrices of random media: means for spectral polarimetric measurements," *Opt. Lett.* **35**, 2236–2238 (2010).
20. Q. Hang et al., "Photonic bandgap fiber bundle spectrometer," *Appl. Opt.* **49**, 4791 (2010).
21. B. Redding and H. Cao, "Using a multimode fiber as a high-resolution, low-loss spectrometer," *Opt. Lett.* **37**, 3384–3386 (2012).
22. B. Redding, S. M. Popoff, and H. Cao, "All-fiber spectrometer based on speckle pattern reconstruction," *Opt. Express* **21**, 6584–6600 (2013).
23. B. Redding et al., "High-resolution and broadband all-fiber spectrometers," *Optica* **1**, 175–180 (2014).
24. M. Piels and D. Zibar, "Compact silicon multimode waveguide spectrometer with enhanced bandwidth," *Sci. Rep.* **7**, 43454 (2017).
25. N. Coluccelli et al., "The optical frequency comb fibre spectrometer," *Nat. Commun.* **7**, 12995 (2016).
26. S. F. Liew et al., "Broadband multimode fiber spectrometer," *Opt. Lett.* **41**, 2029–2032 (2016).
27. M. Mazilu et al., "Random super-prism wavelength meter," *Opt. Lett.* **39**, 96–99 (2014).
28. G. D. Bruce et al., "Overcoming the speckle correlation limit to achieve a fiber wavemeter with attometer resolution," *Opt. Lett.* **44**, 1367–1370 (2019).
29. Y. Li, Y. Xue, and L. Tian, "Deep speckle correlation: a deep learning approach toward scalable imaging through scattering media," *Optica* **5**, 1181 (2018).
30. R. K. Gupta et al., "Deep learning enabled laser speckle wavemeter with a high dynamic range," *Laser Photonics Rev.* **14**(9), 2000120 (2020).
31. L. V. Nguyen et al., "Sensing in the presence of strong noise by deep learning of dynamic multimode fiber interference," *Photonics Res.* **9**, B109–B118 (2021).
32. G. C. Valley, G. A. Sefler, and T. J. Shaw, "Compressive sensing of sparse radio frequency signals using optical mixing," *Opt. Lett.* **37**, 4675–4677 (2012).
33. G. C. Valley, G. A. Sefler, and T. J. Shaw, "Multimode waveguide speckle patterns for compressive sensing," *Opt. Lett.* **41**, 2529–2532 (2016).
34. G. A. Sefler, T. J. Shaw, and G. C. Valley, "Demonstration of speckle-based compressive sensing system for recovering RF signals," *Opt. Express* **26**, 21390–21402 (2018).
35. A. C. Scofield et al., "Recent results using laser speckle in multimode waveguides for random projections," *Proc. SPIE* **10937**, 109370B (2019).
36. J. D. Malone et al., "DiffuserSpec: spectroscopy with Scotch tape," *Opt. Lett.* **48**, 323–326 (2023).
37. N. H. Wan et al., "High-resolution optical spectroscopy using multimode interference in a compact tapered fibre," *Nat. Commun.* **6**, 7762 (2015).
38. A. C. Scofield et al., "Demonstration of GHz-band RF receiver and spectrometer using random speckle patterns," in *Conf. Lasers and Electro-Opt., OSA Tech. Digest*, p. AF2Q.2 (2018).
39. M. J. Kelley et al., "High-resolution broadband RF spectrometer based on laser speckle imaging," *Proc. SPIE* **12225**, 1222503 (2022).
40. M. J. Kelley, T. J. Shaw, and G. C. Valley, "High-speed signal reconstruction for an RF spectrometer based on laser speckle imaging," *Proc. SPIE* **12420**, 124200L (2023).
41. R. Tibshirani, "Regression shrinkage and selection via the lasso," *J. R. Stat. Soc. Ser. B-Methodol.* **58**(1), 267–288 (1996).
42. F. Pedregosa et al., "Scikit-learn: machine learning in Python," *J. Mach. Learn. Res.* **12**, 2825–2830 (2011).
43. G. C. Valley and T. J. Shaw, "Applications of the orthogonal matching pursuit/nonlinear least squares algorithm to compressive sensing recovery," in *Applications of Digital Signal Processing*, C. Cuadrado-Laborde, Ed., pp. 169–190, IntechOpen (2011).
44. H. Cao, "Perspective on speckle spectrometers," *J. Opt.* **19**(6), 060402 (2017).
45. M. N. Ashner et al., "Photonic reservoir computer using speckle in multimode waveguide ring resonators," *Opt. Express* **29**(13), 19262–19277 (2021).
46. EOSPACE Inc.,"EOSpace Website," https://www.eospace.com/short-wavelength-modulator (accessed 19 June 2023).

47. N. Mitsugi, K. Kiuchi, and H. Nagata, "Activation energy for DC-drift in X-cut LiNbO3 optical intensity modulators," *Appl. Opt.* **37**, 8147–8146 (1998).
48. P. S. Devgan et al., "Even-order harmonic cancellation for off-quadrature biased Mach-Zehnder modulator with improved RF metrics using dual wavelength inputs and dual outputs," *Opt. Express* **17**, 9028–9039 (2009).
49. "Photron website," https://photron.com/wp-content/uploads/2024/03/Datasheet_24.03.18.pdf (accessed 8 January 2023).
50. M. J. Murray et al., "High-speed RF spectral analysis using a Rayleigh backscattering speckle spectrometer," *Opt. Express* **31**, 20651–20664 (2023).
51. M. Zhang et al., "Integrated lithium niobate electro-optic modulators: when performance meets scalability," *Optica* **8**, 652–667 (2021).

Matthew J. Kelley is a research scientist at the Aerospace Corporation in the Photonics Technology Department. His interests include microwave photonics, optical time transfer, ultrafast lasers and spectroscopy.

Thomas Justin Shaw: Biography is not available.

George C. Valley is a principal scientist at the Aerospace Corporation where he works on microwave photonics for radio frequency signal detection and processing and memristor-based neuromorphic computing, past work includes photonic compressive sensing, photonic ADCs, Er and Er-Yb fiber amplifiers, photorefractive nonlinear optics, and wave propagation in random media.